LIAD-fs: A novel method for studies of neutral biomolecules in the gas phase

Contact *c.calvert@qub.ac.uk*

CR Calvert, O Kelly, L Belshaw, MJ Duffy, RB King, ID Williams and JB Greenwood

Centre for Plasma Physics,
School of Mathematics and Physics,
Queen's University Belfast

TJ Kelly and JT Costello

National Centre for Plasma Science and Technology,
School of Physical Sciences,
Dublin City University

Introduction

Intense femtosecond (fs) laser pulses provide unique tools for influencing and observing molecular dynamics on ultrashort timescales [1]. Whilst such pulses have been applied for time-resolved studies in the most fundamental molecules (e.g. see [2] and references therein), there is increasing interest in using this technology for studying bond fragmentation in molecules of biological importance. For example, there is significant promise in sequencing of peptides [3] and of selective bond cleavage in prototypal amino acids [4]. We report here on recent experimental studies of fs laser interactions with molecules of biological interest, using the UFL2 laser from the CLF laser loan pool [5]. In a novel experimental approach, LIAD-fs, we used Laser Induced Acoustic Desorption [6] to produce a gas phase target of neutral molecules, which are then exposed to an fs laser pulse with ionisation/fragmentation products subsequently analysed.

Experimental Technique

In order to study fragmentation dynamics for a laser interaction with individual molecules, the ability to produce a gas phase target is paramount. For studies of biomolecules in the gas phase, the pioneering methods of electrospray ionisation (ESI) [5] and matrix assisted laser desorption/ionisation (MALDI) [6] are widely used. These soft ionisation techniques enable studies of thermally labile non-volatile molecules, where ionisation typically occurs via proton/ ion attachment/detachment. While these methods have provided significant progress in studies of biomolecular photoabsorption and fragmentation, there are inherent limitations in their scope. Both ESI and MALDI are restricted to polarised molecules that easily undergo ion/proton attachment/detachment and the created target is thus a modified form of the biomolecule of interest. Also, in MALDI the preparation conditions and the choice of matrix molecule can be very specific to the desired biomolecule target/analyte.

Instead of the commonly adopted ESI or MALDI techniques we use an alternative method of preparing our gas-phase target, that of laser induced acoustic desorption (LIAD). This is a non-destructive desorption method which produces intact, gas-phase molecules with relatively low internal temperatures [8]. Moreover, it allows us to interrogate a *neutral* target of biomolecules, and can be applied for a wide range of molecules. where target preparation conditions are not as sensitive as MALDI.

As depicted in Figure 1, a biomolecular sample (a) is deposited on the surface of a thin Ta foil which is then back-irradiated, using a ns UV pulse (b). This interaction stimulates the propagation of an acoustic wave through the foil, resulting in sample desorption from the surface. After a chosen delay time a femtosecond pulse (c) is then interacted with the desorbed neutral target and ionisation/fragmentation products are extracted and mass analysed (d), via either a time-of-flight (ToF) arrangement or ion trap mass spectrometer [9].

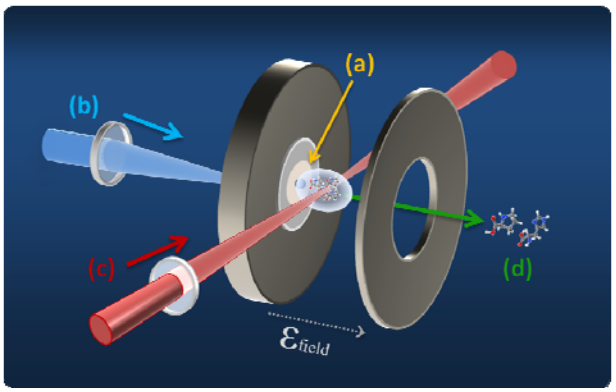

Figure 1: Schematic of LIAD-fs, where a sample is deposited on a Ta foil (a) which is then back-irradiated using a UV ns pulse (b). A femtosecond laser (c) is then interacted with the resulting biomolecular plume, with charged products extracted and analysed electrostatically (d).

The Ta foil, of 10μm thickness and 8mm diameter (Goodfellow®), was secured to the stainless steel electrode in our ToF device using epoxy resin, vacuum compatible glue. Molecular samples were purchased from Sigma-Aldrich®, and typically prepared in 0.01 – 0.05 molar aqueous solution. This solution was deposited on the Ta foil surface in several successive applications, using a vacuum drying station at each stage, with typically 10 – 20 μl deposited in total. For each new sample, a new Ta foil was prepared.

The UV laser pulses used to back-irradiate the foil were produced by an Opotek® Opolette laser, providing 355 nm pulses of ~ 4 ns duration and ~0.3 mJ per pulse which were focused down onto the foil to provide pulse intensities in the range 10^8-10^9 W cm^{-2}. The ns UV laser was synchronised to the UFL2 fs system, a Coherent® Libra regenerative amplifier providing 1mJ pulses at λ = 800 nm and with pulse duration of ~100 fs. Both systems were operated at 20 Hz, with the UV-fs delay (between the Opotek and Libra systems) typically set in the range 10-30 μs. Acquisition for the time-of-flight measurements was triggered using a photo-diode to detect the fs pulse. For the resultant spectra, we have investigated the influence of laser pulse parameters such as UV-fs delay, UV/fs pulse intensity and fs pulse duration on the fragmentation pattern. This has been carried out for a range of small biomolecules, with a few typical results given here.

Results and Discussion

Results from a LIAD-fs study of the amino acid histidine are shown in Figure 2, with the structure of histidine given in the inset ($C_6H_9N_3O_2$, mass = 155 amu). For the results displayed in Figure 2(a), the UV-fs delay was set at 20 μs and the fs pulse was focused onto the neutral plume with a peak intensity of ~5x10^{14} W cm^{-2} (most ions will originate from lower intensities in the focal volume of the laser). It is immediately apparent that the majority of ion signal is detected in the mass range 10 - 50 amu, such that the neutral histidine molecule is being

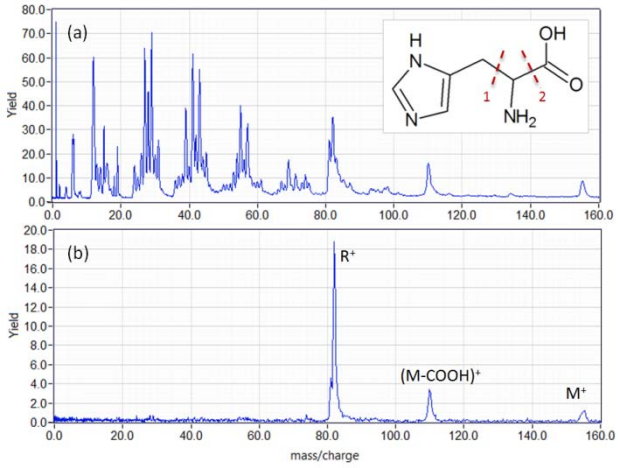

Figure 2: LIAD-fs studies of histidine (structure inset). (a) fs peak intensity ~$5x10^{14}$ W/cm^2 (b) fs peak intensity ~ $1x10^{13}$ W/cm^2.

substantially fragmented. By decreasing the laser intensity, using a cylindrical lens focussing arrangement, the fragmentation pattern can be significantly altered, with lower mass fragments suppressed and three main mass peaks observed in (b). To do this, a diverging cylindrical lens with focal length of 20cm was inserted, decreasing the peak intensity and providing a greater focal volume at low intensities. Under these conditions, the parent ion (M^+) is observed at 155 amu, and the peak at 110 amu is due to the loss of the carboxyl group from the parent ion (breakage of bond 2). The most dominant peak however is that at 81 - 82 amu, which is the sidechain of the amino acid (breakage of bond 1). For mass spectrometry studies, it is clear that the fs interaction enables significant fragments to be observed that can be attributed to the histidine molecule. It has been demonstrated that the laser intensity enables control over the degree of fragmentation.

Results from a LIAD-fs study of another amino acid, Lysine, are shown in Figure 3. Lysine is an essential amino acid for processes such as calcium absorption, building muscle protein and for the production of enzymes and antibodies in the body. It is an α-amino acid with a side chain of $(CH_2)_4NH_2$ and the mass of the parent molecule is 146 amu. At a UV-fs delay of 20 μs and fs intensity of ~10^{13} W cm^{-2}, data was acquired over 2000 laser shots and a number of significant fragments observed.

Similar to the histidine studies, the pulse intensity plays an important role in the degree of fragmentation of the molecule, with this 'low'intensity interaction providing intact fragments from 30 amu upwards. The parent ion is clearly seen at 146, as is the sidechain (peak 5 at a mass of 72 amu). Indeed, moving from high mass to low mass in the Figure, there is evidence for breakage of each bond along the sidechain.

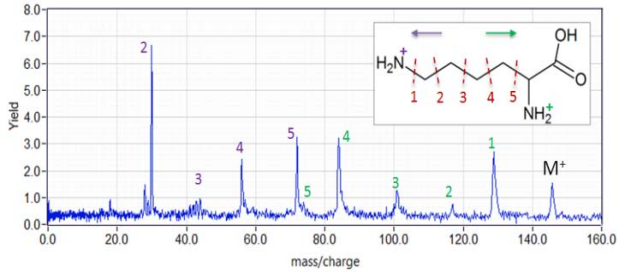

Figure 3: LIAD-fs study of Lysine (mass 146 amu), with fs peak intensity at ~$1x10^{13}$ W cm^{-2}. The peaks are attributed to breakage of bonds 1 to 5, with the colour denoting the location of the charge upon fragmentation.

For ease of reference, we have labeled each bond along the sidechain of the structure from 1 to 5, and annotated the mass peaks accordingly. For each peak, the colour of the number denotes the side of the molecule that is observed, i.e. where the charge resides after fragmentation. For example peak 5 at mass of 72 amu corresponds to a breakage of the bond between sidechain and amino-acid backbone, with the observed fragment being the sidechain (to the left of the bond in the picture). For this particular cleavage, the remainder of the molecule has a mass of 74 amu and there is a small peak observable here (green 5) as a shoulder on the main peak at 72 amu.

Using this notation, it is immediately clear that all bonds along the sidechain can be broken by the fs laser interaction, with the fragments clearly observed. It is worth noting that the C_α-C bond on the amino acid backbone can also be broken (as was seen in histidine), with fragments of 101 amu and 45 amu coinciding with the same mass as the breakage of bond 3. The data in Figure 3 provides a clear 'fingerprint' for the Lysine molecule, such that its fragmentation pattern is well characterized for these LIAD-fs conditions.

In a separate experiment (not shown), a sample was prepared containing both lysine and histidine, and LIAD-fs experiments carried out. The resulting mass spectrum was consistent with a linear combination of the separate fingerprints from Figure 2(b) and Figure 3 here. This demonstrates a useful application of the technique for mass spectrometry, where comparison of an unknown sample with a library of known samples (or 'fingerprints') can enable identification of constituent parts.

Conclusions

The results reported here demonstrate the capability of the novel LIAD-fs technique for creation and ionisation/ fragmentation of a neutral gas phase target of biomolecules. By controlling the fs pulse intensity, we have established that fragmentation can be significantly suppressed.

These formative studies have been carried out using pulses of 100 fs duration, and provide insight into how these small biomolecules behave in an intense laser field. This provides a valuable platform for future studies where ultrashort pulses (< 10 fs) promise to enable observation and control of biomolecular fragmentation on sub-vibrational timescales. In terms of ultrafast dynamics, we are now in a position to carry out pump-probe studies of biomolecules, looking at ultrafast dynamics such as vibrational wavepacket evolution and charge transport [10].

Acknowledgements

CR Calvert acknowledges funding from EPSRC (Postdoctoral Research Fellowship, at the Physics-Life Science interface). O Kelly and RB King acknowledge funding from Leverhulme Trust. L Belshaw and M Duffy acknowledge funding from the Department of Employment and Learning (NI).

This work was carried out using the UFL2 system from the Laser Loan Pool, funded by EPSRC.

References

1. AH Zewail 2000 *J. Phys. Chem. A* Vol 104 Issue 24 5660
2. CR Calvert *et al* 2010 *Phys Rep* Vol 491 Issue 1 pg 1-28
3. CL Kalcic *et al* 2009 *J. Am. Chem. Soc* 131 940
4. T Laarman *et al* 2008 *J. Phys. B.* 41 074005
5. JB Fenn *et al* 1989 Science 246 (4926): 64–71
6. K Tanaka *et al* 1988 Rapid Comm Mass Spec 2 (20) 151–3
7. www.clf.rl.ac.uk/Facilities/Laser+Loan+Pool/14706.aspx
8. AV Zinovev *et al* 2007 *Anal. Chem.* 79 8232
9. JB Greenwood *et al* 2011 *Rev. Sci. Inst.* 82 043103
10. F Remacle and RD Levine 2006 PNAS 103 6793

Photoacoustic Stimulated Raman Spectroscopy (PARS) for Trace Detection of Molecular Hydrogen

Contact Michael Hippler, *M.Hippler@sheffield.ac.uk*

Claire Louise Spencer, Verity Watson and Michael Hippler

Department of Chemistry, University of Sheffield, Sheffield S3 7HF, England

Introduction

New Raman experiments are required for ultra-trace analysis of IR-inactive substances. Trace detection of H_2 is particularly relevant in metallurgy [1]. Exposure of steel or metal alloys to trace amounts of H_2 adversely affects its mechanical properties, since H_2 diffuses easily into the metal, a process which is associated with crack growth and fracture processes. There is a concern that in sensitive environments (power plants, storage of nuclear materials, gas pipelines, etc.), safety could be compromised if steel enclosures are exposed to traces of H_2. Cracking is also a concern for the oil industry since hydrogen as a by-product of corrosion processes can penetrate steel pipelines. With the possible switch from a fossil fuel based energy economy to a hydrogen based economy in the future, there is an increasing need to monitor H_2 with great sensitivity and high selectivity [2]. Unfortunately, H_2 has no permanent or transient electric dipole moment and can not be detected by microwave or IR spectroscopy. H_2 is thus extremely difficult to detect by direct optical absorption techniques. Resonance lines of its electronic spectrum lie in the extreme UV, and rotation-vibration bands and pure rotational lines are IR-inactive. These occur only by quadrupole radiation, where transitions are typically 4-5 orders of magnitude weaker than IR-active electric dipole transitions. The vibrational fundamental band can be more conveniently accessed by Raman spectroscopy. Applications of Raman spectroscopy for the trace gas analysis, however, require special experimental techniques due to the low inherent sensitivity of Raman transitions. New, advanced Raman spectroscopic techniques, however, have the potential to monitor and control IR-inactive substances with great sensitivity and selectivity.

We have recently set up high-resolution stimulated Raman experiments with photoacoustic detection (PARS) which are suitable to detect Raman active molecules in the gas phase [3,4]. With the help of a laser loan from the EPSRC Laser Loan Pool (LP REF No: 92002), two different schemes of stimulated Raman photoacoustic detection of H_2 have been set up and characterized [5], one with a Raman shifter and a second scheme with a tuneable dye laser to generate stimulating Raman excitation. In addition, green Nd:YAG light served as Raman pump radiation. Both beams were focused into a cell with a gas mixture to be analysed. H_2 absorbed radiation due to the stimulated Raman effect, and photoacoustic signals were detected by a microphone.

Stimulated Raman effect using a Raman shifter

The stimulated Raman effect in H_2 with 532 nm as Raman excitation requires radiation around 683 nm for stimulation. One convenient possibility to generate this stimulating radiation is to use a Raman shifter cell filled with H_2. Green light from a Nd:YAG laser (second harmonic 532 nm, up to 350 mJ at 10 Hz repetition rate) is focussed into a home-built Raman shifter, a 70 cm long stainless steel tube with glass windows. Different focusing conditions and H_2 pressures were explored in order to get an approximate 50:50 ratio between unconverted 532 nm light and 683 nm 1st Stokes radiation; the best conditions were achieved with a 1 m focusing lens and 5 bar H_2 filling pressure, giving 14 mJ/pulse green and 18 mJ/pulse red radiation.

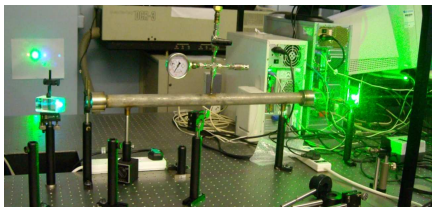

Fig. 1: Photograph showing the Raman shifter in use during experimental set up.

The light was then focused with an 11 cm focal length lens into the centre of photoacoustic cell. Signals from 64 laser shots were averaged for one reading, and each measurement was repeated 9 times, resulting in an overall measurement time of 1 min for an H_2 determination. The photoacoustic cell was filled with a mixture of some mbar H_2 in 1 atm air. Fig. 2 shows that excellent linearity is achieved in the detection of H_2. To obtain a detection limit, a gas mixture without any H_2 has also been measured. The standard deviation of this measurement was taken as a measure of the noise limit of this detection scheme. In addition, a constant background signal is observed in all samples which has to be subtracted from the measurements; it is most likely be due to non-resonant windows signals of the photoacoustic cell. This background has to be subtracted from all measurements. According to the calibration line of fig. 2, the noise equivalent H_2 detection limit is 108 ppm in 1 atm air with this scheme [5].

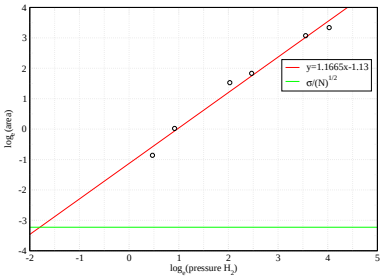

Fig. 2: Double-logarithmic plot of H_2 pressure in 1 atm air vs photoacoustic signal in the non-dispersive scheme. The green line is the noise level.

Note that photoacoustic signals are proportional to the Raman pump and Raman stimulating power. Better sensitivity can thus be achieved by using higher laser powers. Although this scheme is very simple, requiring only one laser of fixed wavelength, it is non-dispersive, however, and lacks the additional benefit of spectroscopic discrimination and selectivity. This also limits the sensitivity which can be achieved, since the noise affected non-resonant background can not be distinguished for each measurement by a spectral baseline.

In previously reported work, Oki et al. [6] have set up a similar detection method for H_2 using PARS with 104 and 44 mJ/pulse for the fundamental (532 nm) and red shifted (683 nm) beams, respectively. A detection limit of 3.4 ppm has been reported which is roughly comparable to the present results considering the much higher power available.

Stimulated Raman spectroscopy of H_2

To overcome the limitations of the non-dispersive scheme, a stimulated Raman photoacoustic experiment has been set up using a tuneable dye laser as Raman stimulating source. The scheme is summarized in fig. 3.

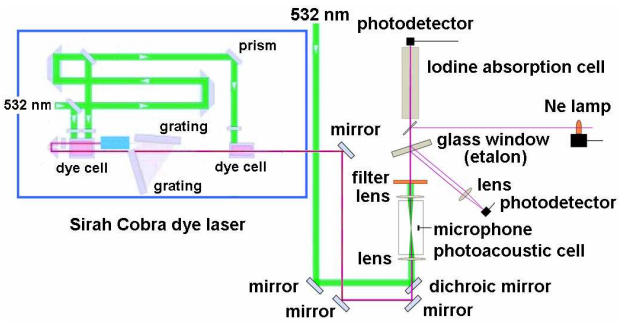

***Fig. 3**: Schematic of stimulated Raman photoacoustic setup.*

In the experiment, ca. 30 mJ/pulse 532 nm laser light (second harmonic of a seeded Nd:YAG laser) is the Raman pump beam which is combined with ca. 35 mJ/pulse tuneable output around 683 nm of a dye laser as the stimulating beam and focused with an 11 cm focal length lens into a photoacoustic cell. If the energy difference between the laser photons corresponds to an allowed Raman transition, molecules are promoted to a vibrationally excited state by the stimulated Raman process. By collisions, the vibrational excitation is converted into local heating which creates a pressure wave which is picked up by a microphone (photoacoustic Raman spectroscopy, PARS). Since the seeded Nd:YAG laser has a very narrow bandwidth, the resolution of stimulated Raman scattering is only limited by the bandwidth of the stimulating dye laser (ca. 0.05 cm^{-1}). More details of this scheme can be found in previous reports [1,2]. Using the tuneable dye laser, Raman spectra of H_2 can be obtained (see fig. 4). A wavelength range of 685 - 682 nm was scanned with the dye laser and four *Q*-branch lines of the fundamental vibration were observed, showing clearly the effect of nuclear spin statistics in H_2 with 1:3 intensity alternations between even and odd *J* lines. The strongest line at room temperature is the *Q*(1) line at 4155 cm^{-1} Raman shift.

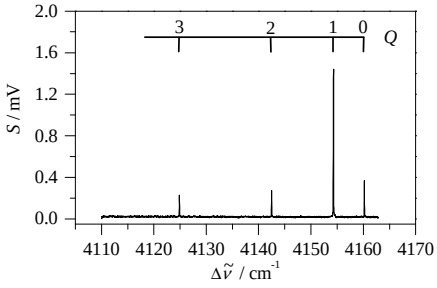

Fig. 4: Q-branch of H_2 (20 mJ green, 20 mJ red per pulse; 86 mb H_2).

To characterize the performance, the photoacoustic cell was filled with some mbar of H_2 in 1 atm air in a dilution series. Integrating the area of the photoacoustic signal of the *Q*(1) line, a signal reading corresponding to a H_2 concentration is obtained in ca. 3 min. Each measurement was repeated 9 times, resulting in an overall measurement time of 30 min for a H_2 determination. Excellent linearity is obtained in this scheme for H_2 detection (see fig. 5). In this scheme, non-resonant background is easily discriminated due to the spectral baseline, and is thus not limiting sensitivity as in the non-dispersive scheme introduced before. The spectroscopic detection has also the significant advantage of additional selectivity. Since the photoacoustic Raman signals depend linearly on the Raman pump and stimulating Raman power, better sensitivities can be achieved in principle with higher power lasers.

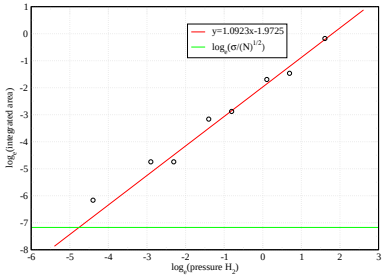

Fig. 5: Double-logarithmic plot of H_2 pressure in 1 atm air vs photoacoustic signal corresponding to the second spectroscopic scheme. The green line is the noise level.

With a noise level determined as the standard deviation of the measurements of air without H_2, the noise equivalent detection limit is determined as 3 ppm H_2 in 1 atm air (see fig. 5). With this high sensitivity and the spectroscopic selectivity, the scheme presented is very suitable for reliable detection of hydrogen in ambient air and gas mixtures. More details on the detection of gas phase molecules by stimulated Raman photoacoustic spectroscopy will be reported in a subsequent full publication [5].

Conclusions

Using a laser loan from the EPSRC Laser Loan Pool, stimulated Raman experiments with photoacoustic detection were set up to detect molecular hydrogen. Two different schemes were evaluated:

In one scheme, a green Nd:YAG laser was focussed into a Raman shifter filled with several bar of H_2. The outgoing radiation contained remaining green light as Raman pump, and red-shifted light as Raman stimulating light. This radiation was focussed into a second cell with a gas mixture to be analysed. H_2 absorbed radiation due to the stimulated Raman effect, and photoacoustic signals were picked up by a microphone with a noise-equivalent detection limit of 108 ppm H_2 in 1 atm air. The method is non-dispersive, however, and lacks spectroscopic discrimination.

To overcome this, in a second experiment a Nd:YAG laser was used as Raman pump, and a tuneable dye laser as stimulating source. Both beams were focused into a photoacoustic cell to analyze gas mixtures. Excellent selectivity was found with a noise-equivalent detection limit of 3 ppm H_2 in 1 atm air. This scheme is thus suitable for reliable detection of hydrogen with high sensitivity and selectivity in ambient air and gas mixtures.

Acknowledgements

A laser loan from the EPSRC Laser Loan Pool (LP REF No: 92002) is gratefully acknowledged. Our work is supported financially by the University of Sheffield.

References

1. P. Doig and G.T. Jones, *Metallurgical and Materials Trans. A* **8**, 1933 (1977); G. M. Bond, I. M. Robertson and H. K. Birnbaum, *Acta Metallurgica* **35**, 2289 (1987).
2. M. Conte, A. Iacobazzi, M. Ronchetti, and R. Vellone, *J. Power Sources* **100**, 171 (2001).
3. M. Hippler and C. Mohr, Central Laser Facility, Rutherford Appleton Laboratory, Annual Report, (2007) 120-123.
4. C.L. Spencer, C. Mohr and M. Hippler, preliminary report in Central Laser Facility, Rutherford Appleton Laboratory, Annual Report, (2010), 27; comprehensive publication in preparation.
5. C.L. Spencer, V. Watson and M. Hippler, to be published.
6. Y. Oki, N. Kawada, T. Ogawa, Y. Abe, M. Maeda; *Jap. J. Appl. Phys.* **36**, 1172 (1997); Y. Oki, N. Kawada, Y. Abe, M. Maeda, *Opt. Commun.* **61** (1999) 57; 7. Y. Oki, S. Nakazono, Y. Nonaka, M. Maeda; *Opt. Lett.* **25** (2000) 1040.

Dynamics of chemical and photochemical reactions in solution

Contact *Professor Andrew Orr-Ewing, Tel: 0117 928 7672, e-mail: A.Orr-Ewing@bris.ac.uk*

S.J. Greaves
School of Chemistry
University of Bristol, Bristol BS8 1TS

R.A. Rose
School of Chemistry
University of Bristol, Bristol BS8 1TS

T.A.A. Oliver
School of Chemistry
University of Bristol, Bristol BS8 1TS

M.N.R. Ashfold
School of Chemistry
University of Bristol, Bristol BS8 1TS

A.J. Orr-Ewing
School of Chemistry
University of Bristol, Bristol BS8 1TS

M. Towrie
Central Laser Facility
STFC Rutherford Appleton Laboratory

G.M. Greetham
Central Laser Facility
STFC Rutherford Appleton Laboratory

I.P. Clark
Central Laser Facility
Rutherford Appleton Laboratory

Introduction

The dynamics of chemical reactions in the gas phase have been widely studied through experimental measurements of quantum-state resolved reactive collisions and computation of potential energy surfaces and the associated reactive scattering. Under conditions of isolated collisions between gas-phase reactants, the distribution of the available energy for the reaction among translational, rotational and vibrational motions of the products can be determined, as can the directions of scatter. From these very detailed outcomes, profound deductions can be made concerning the fundamental mechanisms of chemical reactions. Much of the chemistry of importance in research laboratories, industrial processes, the natural environment, or biological systems occurs, however, in liquid solutions. The presence of a solvent significantly constrains the information that can be extracted from experimental studies of reaction dynamics because the frequent collisions of solvent molecules and solvated reactants or products mask information about the specificity of flow of energy into rotational and vibrational quantum states and translational degrees of freedom.

Although the free rotational and translational motions of a molecule in solution are hindered by the presence of a solvent shell, vibrational motions might only be weakly coupled to the solvent. Ultrafast vibrational spectroscopy therefore offers an opportunity to study how the excess energy of a chemical reaction is channeled into specific vibrational quantum states of the reaction products. The reaction of CN with cyclohexane

$$CN + c\text{-}C_6H_{12} \rightarrow HCN + c\text{-}C_6H_{11} \qquad (1)$$

serves as an illustration. This reaction is exothermic by ~ 10000 cm^{-1} and the HCN product possesses three vibrational modes well-described in a local mode picture as a C-N stretch (ν_1 = 2128 cm^{-1}), a bend (ν_2 = 727 cm^{-1}) and a C-H stretch (ν_3 = 3444 cm^{-1}). The values in parentheses are the harmonic vibrational frequencies of isolated HCN, and it is known from spectroscopic studies of this reaction in the gas phase that much of the excess energy is efficiently coupled into C-H stretching and bending excitation of the HCN, with sufficient energy available to excite several vibrational quanta. To what extent such vibrational mode-specific dynamics can persist in solution is one of the main questions addressed by this project. Comparisons with the known dynamics of the gas-phase reaction then provide an unprecedented opportunity to examine the role of the solvent in the microscopic mechanism of a chemical reaction in solution.[1,2]

Experiment

Experiments were carried out at the ULTRA laser system at the Rutherford Appleton Laboratory. A ~50 fs ultra-violet (UV) laser pulse with wavelength of 266 nm was used to generate CN radicals from the photodissociation of ICN. In the presence of cyclohexane, HCN was formed by reaction (1) and a ~ 1 ps duration infra-red (IR) pulse, time delayed from the UV laser pulse by 1–1000 ps, probed this reaction product. Experiments were carried out in a solvent (one of $CHCl_3$, $CDCl_3$ or CH_2Cl_2) selected so that the IR transitions of the HCN were not masked by solvent absorption bands. Samples were flowed through a cell consisting of two UV and IR-transparent windows (either CaF_2 or BaF_2) separated by 0.4 mm, and the two laser beams were overlapped in the centre of this cell. Typical sample concentrations were 0.14 M ICN and 1.0 M cyclohexane in the chlorinated solvent. A key feature that enabled the experiments is the broad (~500 cm^{-1}) bandwidth of the IR laser pulses. After passing through the sample, the probe IR pulses were dispersed onto two 128-pixel array detectors allowing IR absorption spectra to be captured for each laser pulse. Extensive averaging and accumulation of spectra at numerous time delays between the UV and IR laser pulses allowed measurement of the time-dependence of the HCN vibrational absorption spectrum.

Results and Discussion

Measurements were made of the transient IR absorption spectra of HCN products of reaction (1) and the DCN products of the equivalent reaction of CN with d_{12}-cyclohexane, and illustrative examples are presented here.[1] Time-dependent IR spectra were obtained in the C-H stretching region of HCN (~3250 cm^{-1} in the solvents used), the C-D stretching region of DCN (~2600 cm^{-1}) and the C-N stretching region (~2095 cm^{-1} in HCN and 1925 cm^{-1} in DCN), and additional features assigned as INC and CN complexed to solvent molecules were also observed in the ~2050 cm^{-1} region. Figure 1 shows representative spectra of HCN formed by reaction (1) in CH_2Cl_2, in the 3200 cm^{-1} region at various time delays between the UV photolysis and IR probe lasers. The combs above the spectra indicate the spectroscopic transitions and hence the vibrational levels from which the IR absorption features originate. The assignments are based on careful wavenumber calibration of the pixel scale, and calculation of vibrational transition wavenumbers using harmonic frequencies and anharmonic corrections derived from

high-resolution spectroscopy in the gas phase, together with solvent shifts deduced from the positions of the fundamental transitions. The assignments use the notation (n_1,n_2,n_3), with n_1, n_2 and n_3 denoting, respectively, the number of quanta of vibration of the C-N stretch, the bend and the C-H stretch.

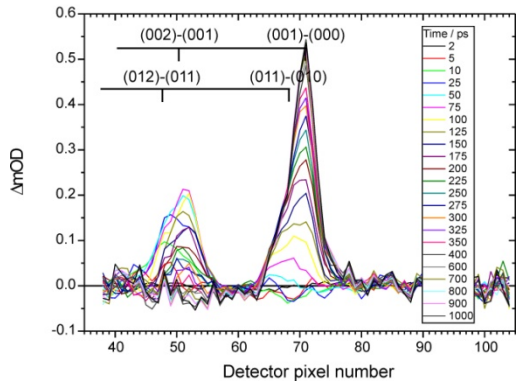

Figure 1: Time-dependent IR spectra in the 3200 cm^{-1} region of HCN formed from reaction (1) in CH_2Cl_2. The combs provide band assignments. Time delays from the UV photolysis to the IR probe laser are shown in the inset.

Several remarkable observations derive from spectra such as those shown in figure 1. It is evident that, despite the presence of the solvent, the nascent HCN is formed with considerable vibrational excitation, up to n_3 = 1 in the C-H stretching mode and n_2 = 2 in the bending mode. Furthermore, the spectra obtained at short time delays between the UV and IR lasers indicate that the majority of the HCN molecules possess one quantum of C-H stretching excitation, and that this relaxes to the vibrational ground state as the time delay increases. The vibrational relaxation is likely to be via dissipation of energy to solvent molecules. The above observations can be made more quantitative by integrating the IR bands to obtain time-dependent intensities. Figure 2 shows the outcomes of such an analysis applied to the spectra in figure 1.

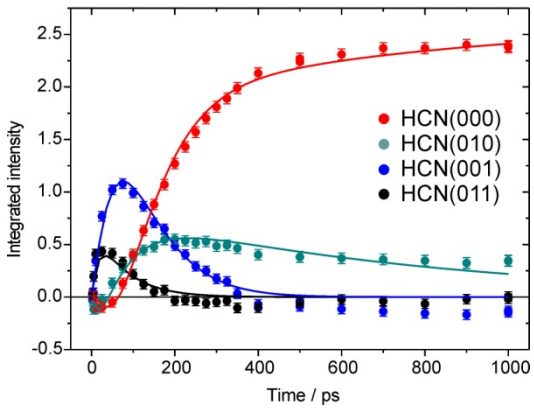

Figure 2: Time-dependence of the intensities of absorption bands observed in the transient IR spectra of HCN formed by reaction (1).

The time-dependent intensity data plotted in figure 2 show clearly the formation of vibrationally excited HCN at early times, and the relaxation to the ground vibrational level at longer time delays. The rates of the vibrational relaxation are observed to depend on the solvent, and independent measurements of the first-order rate coefficients for the vibrational relaxation, using transient IR-pump and IR-probe spectroscopy methods for HCN solutions in the various solvents confirm this interpretation of the observed kinetics.[1]

The data shown in figures 1 and 2 were obtained at IR wavelengths corresponding to the C-H stretching region of HCN, and bending vibrational excitation manifests itself as vibrational hot bands in combination with the C-H stretch. Measurements made in the C-N stretch absorption region are consistent with these C-H region data, and show no clear evidence for C-N stretch excitation. Analysis in this region is complicated, however, by overlap of additional transient IR absorption bands that are assigned to INC (formed by recombination of I atoms and CN radicals following ICN photolysis) and CN weakly complexed to solvent molecules.

The curves through the data points in figure 2 are the result of a fit to a kinetic model that considers reaction dynamics that form HCN (n_1,n_2,n_3) with n_1 = 0 (i.e. the C-N bond is a spectator to the reaction and is not vibrationally excited), n_2 = 1 and 0, and n_3 = 1 and 0. The model also incorporates vibrational energy transfer to the solvent, with the assumption of stepwise loss of single quanta of vibrational energy (i.e. $\Delta n_i = -1$, with i = 2, 3). The rate coefficients that are derived from fits such as those shown in figure 2 quantify the branching between dynamical pathways that form HCN in different vibrational quantum states, and the dependence of these dynamics on choice of solvent.

Detailed interpretation of the experimental results quantified the effect of the solvent on the potential energy surface for reaction (1), and examined the associated chemical dynamics by propagation of classical trajectories in the presence of solvent molecules.[3] Results from these calculations indicate that the transfer of the H atom from cyclohexane to the CN radical occurs at an H–CN distance greater than the equilibrium bond length in HCN and over a wide range of bending angles, which accounts for the efficient excitation of the C–H stretching and bending vibrational modes in reaction (1). It is also clear that the dynamics of reaction (1) in the chosen solvents do not differ markedly from those in the gas phase: the solvent quenching of vibrational excitation occurs on a timescale longer than the reactive collisions. Furthermore, the combination of experimental and computational results demonstrates that the relaxation of the excited HCN to equilibrium departs from the expectations of linear response behaviour.[4] Whether such conclusions persist for solvents that interact more strongly with the CN and HCN solutes remains to be established, and data have been acquired and analysed for reactions in tetrahydrofuran to address this question.

Conclusions

The transient IR absorption capabilities of the ULTRA laser system have been exploited to demonstrate, for the first time, vibrational mode specificity in the release of the excess energy of a bimolecular reaction in solution. The observed formation of nascent HCN with excitation of its bending and C-H stretching vibrational modes and the subsequent relaxation of this vibrational excitation by coupling to the solvent are unique results that provide unprecedented opportunities to study chemical reaction dynamics in liquid solutions and to quantify the effects of the solvent on microscopic reaction mechanisms.

Acknowledgements

The Bristol group gratefully acknowledges financial support from the EPSRC Programme Grant EP/G00224X. SJG thanks the Leverhulme Trust for an Early Career Research Fellowship.

References

1. S.J. Greaves, R.A. Rose, T.A.A. Oliver, D.R. Glowacki, M.N.R. Ashfold, J.N. Harvey, I.P. Clark, G.M. Greetham, A.W. Parker, M. Towrie and A.J. Orr-Ewing, *Science* **331**, 1423 (2011).

2. A.J. Orr-Ewing, D.R. Glowacki, S.J. Greaves and R.A. Rose, *J. Phys. Chem. Lett.* in press (2011).

3. D.R. Glowacki, A.J. Orr-Ewing and J.N. Harvey, submitted (2011).

4. D.R. Glowacki, R.A. Rose, S.J. Greaves, A.J. Orr-Ewing and J.N. Harvey, submitted (2011).

Picosecond Time-Resolved Infrared Spectroscopy of Arylpentazole

Contact *p.portius@sheffield.ac.uk*

Dr. Peter Portius

Dr. Martin Davis

Department of Chemistry
University of Sheffield
Brook Hill

Sheffield S3 7HF, UK

Prof. Mike Towrie

Central Laser Facility
STFC Rutherford Appleton Laboratory

Harwell Science and Innovation Campus

Didcot OX11 0QX, UK

Introduction

Nitrogen-rich molecules are important for chemical energy storage and have a major advantage over conventional solutions to the problem of chemical energy storage, since their decomposition releases almost exclusively the environmentally friendly dinitrogen.[1] In search for stable compounds with high nitrogen content, methods have to be found which allow the introduction of nitrogen in synthetic procedures. The most relevant of these have traditionally been the coordination of the azido anion (N_3^-) to main group elements[2] or the derivatisation of tetrazoles[1, 3] (R-CN_4-R'). Meanwhile, the scope of these methods has been largely realized and forms the basis of various successful applications. For a further increase of nitrogen content, however, new systems have to be identified. A promising avenue in this direction are all-nitrogen species larger than N_3, which could act as ligands. There is a only a surprisingly small number of all nitrogen species known: N_2, N_3^-,[4] N_3 radical ,[5] N_5^+ [6] and the disputed cyclic pentazolate anion *cyclo*-N_5^-.[7] A previously investigated route to *cyclo*-N_5^- involved mass spectrometry of fragments produced by laser desorption ionization (λ = 337 nm)[8] or reduction of the aryl pentazole *para*-Me_2N-C_6H_4-N_5 using cerium ammonium nitrate (CAN).[9] It has been hypothesised that the *cyclo*-N_5^- anion can act as a two-electron donor ligand (N_3^- analog[10]) and as a six-electron donor ligand (Cp^- analog[11]); however, the anion is unavailable in sufficient quantity in order to test this hypothesis experimentally. The TRIR spectroscopy experiments with pentazoles described here were performed in order to photochemically characterise these unusual molecules in general, and explore possibilities for cleaving the aryl-N_5 bond and photochemically generate N_5^- in particular.

Aryl pentazoles

So far, all investigated aryl pentazoles (see Scheme 1)[12] are thermolabile and decompose rapidly at r.t. A σ electron withdrawing and π electron donating substituent in *para* position has been found to increases the stability such that for instance solutions of *para*-Me_2N-C_6H_4-N_5 are stable for many hours at a temperature of –30°C.

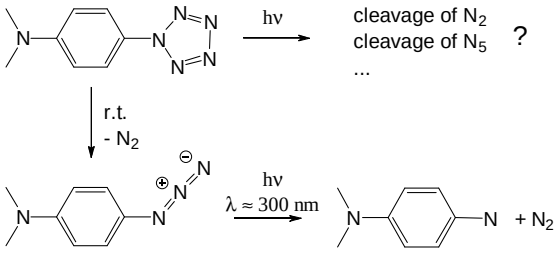

Scheme 1. Reactivity of *para*-Me_2N-C_6H_4-N_5 (top right).

The thermally induced decomposition of the pentazole *para*-Me_2N-C_6H_4-N_5 generates N_2 and the azide *para*-Me_2N-C_6H_4-N_3. The photochemistry of organic azides is generally well investigated and features the loss of N_2 and the formation of a nitrene (see Scheme 1). [13]

Set-up for low-temperature picosecond-TRIR

In order to avoid thermal decomposition and allow TRIR measurements in cases of incomplete photoreversibility, both sufficiently low temperatures, typically between –40 and –30°C, and a continuous exchange of the irradiated solution must be ensured. For this purpose a new flow system was designed and built at the LSF (Scheme 2).

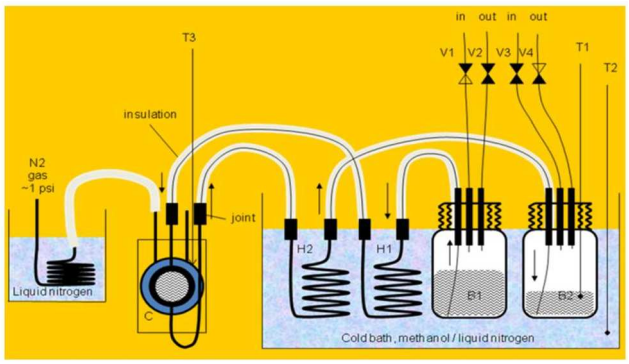

Scheme 2. *Design of the flow system for low temperature picosecond-TRIR as integrated in the ULTRA facility; V1-V4 solenoid valves applying N_2 pressure (0.3 bar) or releasing pressure from the reservoir bottles B1 and B2, H1 and H2 heat exchange coils, T1-T3 thermocouples, C commercial variable temperature spectroscopic cell. The arrows indicate the direction of flow when V1(in)&V4(out) are open and V2&V3 closed.*

This system maintains a flow of cold solution through a variable temperature spectroscopic cell (CaF_2 windows) in a forward / backward fashion via valve controlled alternating pressure in the bottles B1 and B2. The valves V1 to V4 are controlled by an extension to the data acquisition software for the ULTRA laser system[14] and regulate the nitrogen pressure in both bottles such that the flow of cold solution reverses before either bottle B1 or bottle B2 empties completely. The temperature of the irradiated solution is measured by a thermocouple in direct contact with the solution inside the spectroscopic cell and can be regulated between –50°C and ambient by adjusting cold bath temperature and heater current of the spectroscopic cell. The windows of the cell are kept ice-free by a dry nitrogen purge. With this setup solutions of pentazole can be kept undecomposed for many hours.

Time-resolved infrared (TRIR) spectroscopy of *para*-(dimethylamino)phenyl-pentazole, *para*-Me_2N-C_6H_4-N_5

The molecule *para*-Me_2N-C_6H_4-N_5[15] has no characteristic group vibrations and any investigation in the infrared must therefore rely entirely on the fingerprint region, in which strong solvent absorption bands are also present. However, using a set of solvents we were able to monitor picosecond transient IR spectra throughout the range 1250 to 1700 cm^{-1}. The ground state IR spectrum was assigned tentatively with the help of frequency calculations within density functional theory (DFT) at the B3LYP/6-311G(d,p) level. In the TRIR spectra obtained

at −40°C in CH_2Cl_2 solution, five IR absorption bands arising from the *para*-Me_2N-C_6H_4-N_5 ground state can be discerned at 1384, 1485, 1524, 1533 and 1608 cm^{-1}, all of which are fully bleached at 4 ps, whilst a set of transient bands appears at 1304, 1376, 1477 and 1598 cm^{-1}(Fig. 1, Table 1).

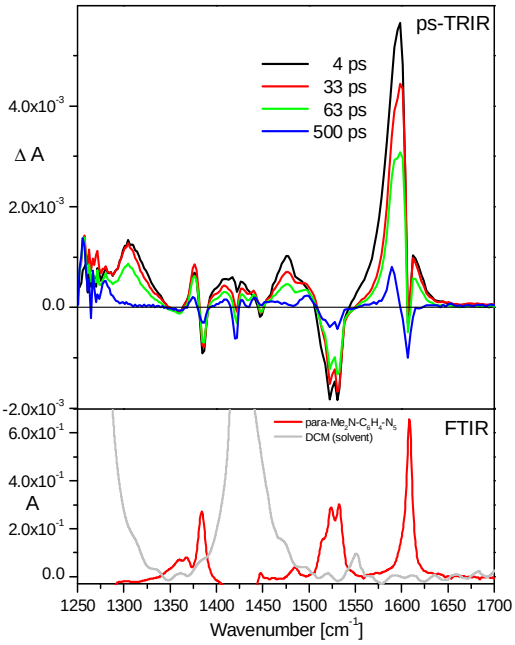

Figure 1. *Low-temperature picosecond-TRIR spectra of a solution of para-Me_2N-C_6H_4-N_5 in CH_2Cl_2 4, 33, 63 and 500 ps after excitation, λ_{exc} = 310 nm (top) obtained with ULTRA; IR difference spectrum showing the ground state IR spectrum of para-Me_2N-C_6H_4-N_5 (bottom, red) and the IR spectrum of the solvent (bottom, grey).*

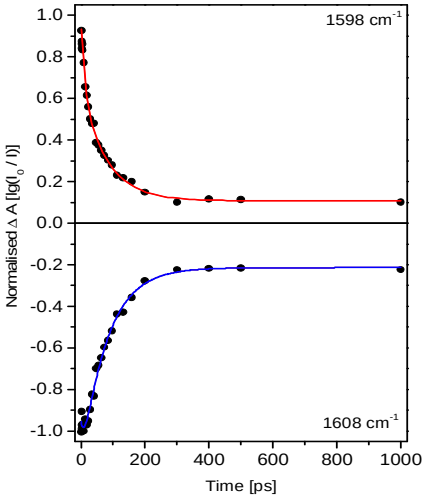

Figure 2. *Normalised kinetic traces showing the complete decay of selected transient bands centred at 1598 cm^{-1} of the excited singlet state (top) and at 1530 cm^{-1} of the ground state of para-Me_2N-C_6H_4-N_5 (bottom), respectively, in CH_2Cl_2 solution at low temperature.*

Table 1. Vibrational frequencies [cm^{-1}].*

	para-Me_2N-C_6H_4-N_5	*para*-Me_2N-C_6H_4-N_5	*para*-Me_2N-C_6H_4-N_3	*para*-[Me_2N-C_6H_4-N_5]*	*para*-[Me_2N-C_6H_4-N_5]*
	TRIR/FTIR	calcd.[a]	FTIR	TRIR	calcd.[a]
1	1608vs	1605vs	1611w	1598vvs	1574vvs
2	1533m	1514vs	1514vs	1477w	1478w
3	1524m	-	-	-	-
4	1485vw	1487vw	-	-	-
5	1384m	1365m	1357vw	1376vw	1359vw
6	-	-	-	1304w	1285w

*) *vs very strong, s strong, m medium, w weak, vw very weak; the calculated wavenumbers are scaled.*

The frequency calculations predict the positions of band maxima and absorption intensities with reasonable accuracy as can be gleaned from a comparison of predicted and observed parameters for the ground state (Table 1). Assuming conservation of electron spin, a geometry optimization and frequency calculation of the lowest singlet excited state, *para*-[Me_2N-C_6H_4-N_5]*, was carried out using DFT. Again, the predicted frequencies and intensities of the prominent transient bands and the observed spectral features can be matched approximately. Due to well-known limitations in DFT[16] the predicted vibrational frequencies and IR intensities are not precise; however, the trends are likely to be predicted accurately. For instance, an extremely strong band is predicted at 1574 cm^{-1}, slightly lower in energy than the related ground state bleach at 1605 cm^{-1}, which indeed is observed (1598 vs 1608 cm^{-1}), whereas for the lowest triplet excited state the respective transient band is predicted at a higher energy (not observed). Thus, the TRIR experiment affords the evidence for the formation of the singlet excited state of *para*-[Me_2N-C_6H_4-N_5] pentazole under 310 nm excitation.

TRIR dynamics

para-[Me_2N-C_6H_4-N_5]* is formed with excess vibrational energy. As a result, a slight band narrowing and a fast decay component of 15(±4) ps can be observed on the low energy side of the main transient band centred at 1598 cm^{-1}. Intriguingly, as much as 78% of the excited *para*-Me_2N-C_6H_4-N_5 recovers to the ground state within the first 300 ps (Fig. 2, Scheme 3), with the lifetimes of both the parent recovery at 1608 cm^{-1} and the excited state decay at 1598 cm^{-1} being identical and equal to 78(±4) ps. Within the accuracy of the experimental data, the remaining transient bands and parent bleaches (Table 1) exhibit identical temporal behavior. In a control experiment, the related azide *para*-Me_2N-C_6H_4-N_3 was investigated by TRIR (λ_{exc} = 310 nm). The parent bleaches of the latter were found to not recover at all on the picosecond time scale. These findings reveal a fundamental difference in the photochemistry of *para*-Me_2N-C_6H_4-N_5 in comparison with the related *para*-Me_2N-C_6H_4-N_3.

Variable low temperature picosecond TRIR experiments with a solution of *para*-Me_2N-C_6H_4-N_5 using the same excitation wavelength show that the singlet excited state lifetime has only weak temperature dependence in the range −41 to 0°C.

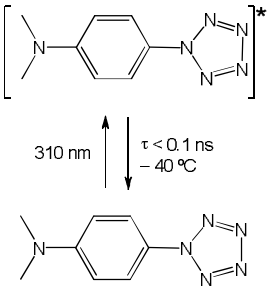

Scheme 3.

As can be deduced from the TRIR spectrum 500 ps after laser flash (Scheme 1, blue spectrum) and from the kinetic trace of the parent bleach at 1608 cm^{-1}, a minor part of photoexcited *para*-Me_2N-C_6H_4-N_5 forms a long lived photoproduct. Correspondingly, weak residual transient bands and parent bleaches are persistent even at 1000 ps. The nature of this long lived photoproduct is currently unknown. It should be pointed out that this product cannot arise from a photoreaction involving the azide *para*-Me_2N-C_6H_4-N_3, which is potentially present as a result of thermal decomposition of the pentazole and which also absorbs at 310 nm, since a corresponding intense bleach at 1514 cm^{-1} (Table 1) is absent from the spectra. *para*-Me_2N-C_6H_4-N_3 itself, formed by a potential photoinduced cleavage of N_2 from *para*-Me_2N-C_6H_4-N_5, can also be excluded from the list of candidate species due to the absence of a (positive) transient band centred at the same spectral position (1514 cm^{-1}). However, the cleavage of the aryl-N_5 bond cannot be ruled out.

Conclusions

The capabilities of ULTRA were extended to low temperatures and the first TRIR spectroscopy experiments involving pentazoles were carried out successfully. The nature of the excited state of *para*-Me_2N-C_6H_4-N_5 was determined in combination with theoretical methods. A long lived photoproduct of yet undetermined nature is formed with a yield of approximately 22%.

Acknowledgements

The authors acknowledge the support of the STFC council via the programmatic access to the ULTRA facility under the proposal “Real-time Structural dynamics of Molecular Systems for Energy Generation and Storage”, P. Portius, J. Weinstein, M. Towrie and the EPSRC for an advanced research fellowship (PP, E054978/1). I. P. Clark, B. Coles and G. Greetham are thanked for their assistance in the cell design and the performance of the experiments. A. H. J. M. Meijer, Sheffield, performed the DFT calculations.

References

[1] Steinhauser, G.; Klapoetke, T. M., *Angew. Chem. Int. Ed.* **2008**, *47*, 2-20.

[2] a) Portius, P.; Filippou, A. C.; Schnakenburg, G.; Davis, M.; Wehrstedt, K.-D., *Angew. Chem. Int. Ed.* **2010**, *49*, 8013-8016; b) Mueller, J., *Coord. Chem. Rev.* **2002**, *235*, 105-119; c) Banert, K.; Joo, Y.-H.; Rüffer, T.; Walfort, B.; Lang, H., *Angew. Chem.* **2007**, *119*, 1187-1190.

[3] a) Singh, R. P.; Verma, R. D.; Meshri, D. T.; Shreeve, J. M., *Angew. Chem. Int. Ed.* **2006**, *45*, 3584-3601; b) Stierstorfer, J.; Tarantik, K. R.; Klapoetke, T. M., *Chemistry--A European Journal* **2009**, *15*, 5775-5792.

[4] Curtius, T., *Ber. Dtsch. Chem. Ges.* **1890**, *23*, 3023 - 3033.

[5] Singh, A.; Koroll, G. W., *Radiat. Phys. Chem.* **1982**, *19*, 137-146.

[6] Haiges, R.; Schneider, S.; Schroer, T., Christe; K. O., *Angew. Chem. Int. Ed.* **2004**, *43*, 4919-4924.

[7] a) Butler, R. N.; Hanniffy, J. M.; Stephens, J. C.; Burke, L. A., *J. Org. Chem.* **2010**, *74*, 1354-1364; b) Schroer, T.; Haiges, R.; Schneider, S.; Christe, K. O., *Chem. Commun.* **2005**, 1607-1609.

[8] Östmark, H.; Wallin, S.; Brinck, T.; Carlquist, P.; Claridge, R.; Hedlund, E.; Yudina, L., *Chem. Phys. Lett.* **2003**, *379*, 539-546.

[9] Butler, R. N.; Stephens, J. C.; Burke, L. A., *Chem. Commun.* **2003**, 1016-1017.

[10] Straka, M.; Pyykko, P., *Inorg. Chem.* **2003**, *42*, 8241-8249.

[11] Frunzke, J.; Lein, M.; Frenking, G., *Organometallics* **2002**, *21*, 3351-3359.

[12] Ugi, I., *Comprehensive Heterocyclic Chemistry* **1984**, *5*, 839.

[13] Braese, S.; Banert, K., ed., *Wiley* **2010**, *Organic Azides*, 311-364.

[14] Greetham, G.; P, B.; A., C. Q.; Clark, I. P.; Codd, P. S.; Farrow, R. C.; George, M. W.; Kogimtzis, M.; Matousek, P.; Parker, A. W.; Pollard, M. R.; Robinson, D. A.; Xin, Z.-J.; Towrie, M., *Appl. Spectrosc.* **2010**, *64* 1311-1319.

[15] Ugi, I.; Perlinger, H.; Behringer, L., *Chem. Ber.* **1958**, *91*, 2324-2329.

[16] a) Johnson, B. G.; Gill, P. M. W.; Pople, J. A., *J. Chem. Phys.* **1993**, *98*, 5612-5625; b) Andersson, M. P.; Uvdal, P., *J. Phys. Chem. A* **2005**, *109*, 2937-2941.

Isotopic hydration of cellobiose: vibrational spectroscopy and dynamical simulations

Contact *John.Simons@chem.ox.ac.uk*

John P Simons, Nitzan Mayorkas

University of Oxford
Physical and Theoretical Chemistry Laboratory, South Parks Road, Oxford OX1 3QZ (UK)

Benjamin G Davis

University of Oxford
Chemistry Research Laboratory, Mansfield Road, Oxford OX1 3TA, UK

Emilio J Cocinero

University of Bilbao

Departamento de Química Física, Facultad de Ciencia y Tecnología, Universidad del País Vasco, (UPV – EHU), Apartado 644, E-48940, Bilbao, Spain

Madeleine Pincu, R Benny Gerber

University of California, Irvine
Department of Chemistry, University of California, Irvine, CA 92697, USA

Brina Brauer

The Hebrew University
Institute of Chemistry and The Fritz Haber Research Center, The Hebrew University, Jerusalem 91904, Israel

Introduction

The factors which dictate the conformational preferences of cellobiose, Glc*p*-β1,4-D-Glc*p*, the basic repeat structural unit of cellulose, remain something of an enigma. *Ab initio* and density functional theory (DFT) calculations of its intrinsic conformation, isolated in the gas phase, predict a *cis* configuration about the glycosidic linkage, i.e. one in which the two dihedral angles, ϕ and ψ, defined in Figure 1, adopt *anti*-ϕ and *syn*-ψ orientations and the two neighbouring hydroxymethyl groups are linked through an inter-ring hydrogen bond. In aqueous solution however, NMR measurements together with molecular dynamics simulations, indicate an average *trans* (*syn*-ϕ, *syn*-ψ) structure about the glycosidic linkage in cellobiose; the *trans* structure is supported by inter-ring hydrogen bonding between OH3 and O5', see Figure 1. in the cellulose polymer the *trans* orientation of the β1,4 linked cellobiose sub-units creates an alternating structure, supported by an extended chain of OH3-O5' hydrogen bonds.

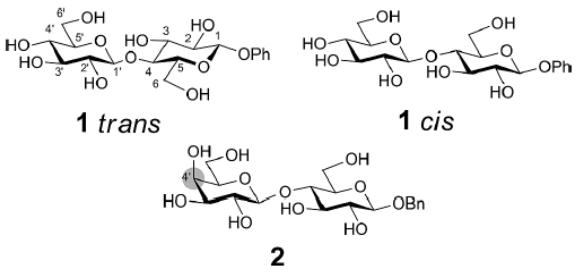

Figure 1. Structural representations of phenyl β cellobioside, 1, and also benzyl β lactoside, 2, shown in its *cis* conformation; lactose is the C4' epimer of cellobiose. The phenyl 'tag' provides the UV chromophore required for implementing the double resonance, IR-UV detection scheme. (Glycosidic dihedral angles are defined as ϕ: H1'-C1'-O-C4 and ψ: C1'-O-C4-H4).

Is the change from the intrinsic *cis* conformation of cellobiose at low temperatures in the gas phase, to the *trans* conformation in condensed phases, associated with an aqueous environment, explicit solvation, the raised temperature, or perhaps all three? Is the *trans* orientation of the cellobiose sub-units in cellulose actively created during its biosynthesis when the glucose units are successively added to the growing β1,4 linked chain, or is it accessed by relaxation of *cis* oriented cellobiose units at the growing terminus, perhaps through explicit hydration or other intermolecular interactions?

Its explicit hydration has now been investigated in the gas phase through double resonance, IR-UV vibrational spectroscopy conducted under molecular beam conditions, substituting D_2O for H_2O to separate isotopically, the carbohydrate (OH) bands from the hydration (OD) bands. Structural assignments have been based on comparisons between the experimental OH vibrational spectrum and the results of DFT and *ab initio* calculations. Complementary Car-Parrinello (CP2K) simulations, employing dispersion corrected DFT potentials and conducted 'on-the–fly' from ~20K to ~300K, have also been used to explore the consequences of raising the temperature.[1]

Vibrational spectroscopy at low temperature

The vibrational spectra of phenyl β cellobioside and its hydrated complexes, phenyl β cellobioside•$(D_2O)_{1,2}$, recorded in a molecular beam environment, are shown in Figure 2 together with their calculated (DFT//MP2) minimum energy structures and the corresponding vibrational spectra: the experimental and calculated spectra are all in good accord.

The *cis* (*anti*-ϕ, *syn*-ψ) conformation of the bare molecule is supported by two inter-ring hydrogen bonds, OH6'→O6 and OH2'→O3 and this bonding is retained in the mono-hydrate, phenyl β cellobioside•D_2O. The reversed orientation of the peripheral OH groups from counter clockwise to clockwise, provides a favoured 'water binding pocket' at the 4',6' site where the bound water molecule can insert to complete the cooperative hydrogen-bonded chain, OH2→ OH3→ OH2'→ OH3'→ OH4'→ W→ OH6'→ OH6 (recalling the behavior of the singly hydrated monosaccharide, phenyl β D-glucopyranoside•H_2O).

It might be thought that the addition of a second water molecule would follow a similar rule. In doubly hydrated phenyl β D-glucopyranoside, the two water molecules add sequentially, with the first occupying the 4,6 site as before and the second located in the vacancy on the other side of the hydroxymethyl group, at the 6,5 site.[2] In phenyl β cellobioside however, the corresponding 6',5' site would be blocked by the inter-ring hydrogen bond, OH6'→OH6, though

the 6,5 site on the neighbouring ring could provide an alternative. The DFT calculations do indeed predict two such structures, but at energies 4.3 and 4.9 kJ mol^{-1} above that of the global minimum. The vibrational spectrum associated with the latter structure, shown in Figure 2, is in very good accord with the experimental spectrum and instead of binding two separate water molecules, the cellobiose unit accommodates a dimer. It links O6' (acting as the hydrogen bond acceptor) and OH3 (acting as the donor) to provide a diagonal bridge across the two rings. The glycosidic conformation of the cellobiose unit remains *cis* however, and its framework structure is very similar to that of the bare molecule, again supported by two inter-ring hydrogen bonds, OH6'→O6 and OH2'→OH3.

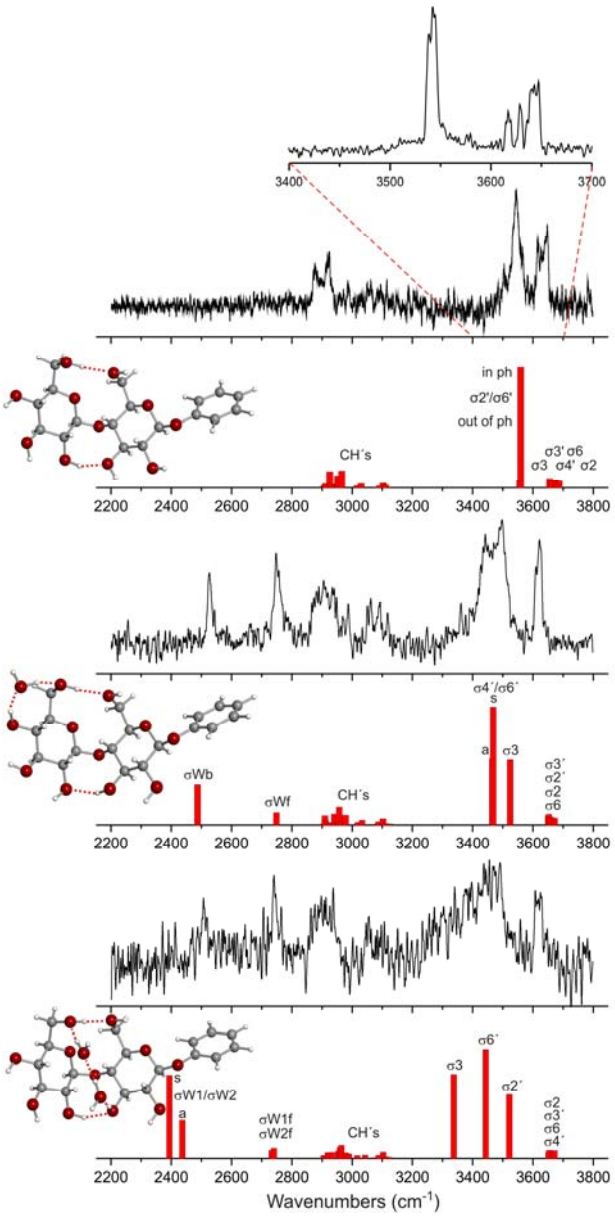

Figure 2. Experimental and (DFT) computed IR spectra and the corresponding hydrogen-bonded molecular structures of phenyl β cellobioside (top), phenyl β cellobioside•D_2O (middle) and phenyl β cellobioside•$(D_2O)_2$ (bottom).

The advantage of using D_2O rather than H_2O, to separate the hydrate (OD) region of the IRID spectrum from the crowded OH region associated with the carbohydrate, is again well demonstrated by the IR spectrum of phenyl β lactoside•D_2O shown in Figure 3. The complexity of the congested spectrum associated with the corresponding H_2O complex (reported earlier [3]) appeared to be incompatible with its assignment to a single structure. The new spectrum confirms the earlier tentative conclusion that it is generated by the two lowest energy structures, shown in Figure 3, which are both populated in the cold molecular beam. The two bands at ~2420 cm^{-1} and ~2530 cm^{-1}, are associated with the bound OD modes, labeled σWb in Figure 3. In the former case, the OD is bound to O6' on the exocyclic hydroxymethyl group, which is then bound, *via* OH6 acting as a donor, to O6' through an inter-ring hydrogen bond. In the latter case, the (lactose) OH groups adopt a reversed, clockwise orientation, and OH6 becomes a hydrogen bond donor to D_2O and there is a (weaker) bond linking OD to O5.

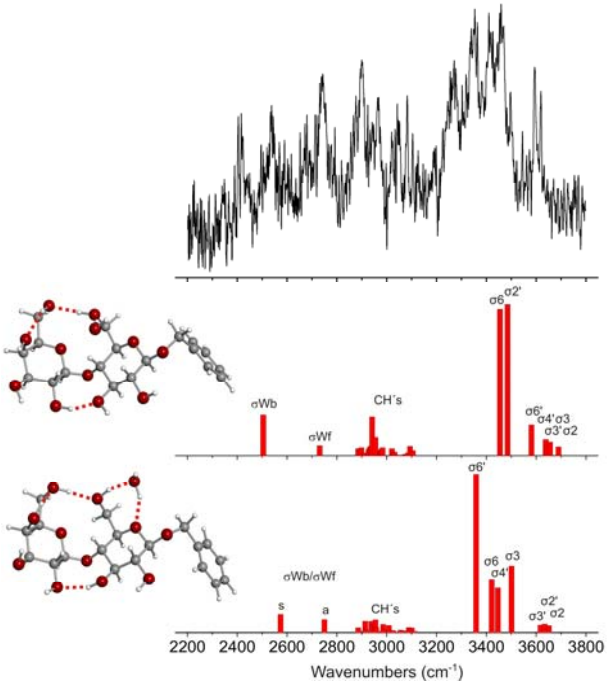

Figure 3. : Experimental and (DFT) computed IR spectra and corresponding hydrogen-bonded molecular structures of the two lowest energy structures of benzyl β lactoside•D_2O: the labels σWf and σWb identify the vibrational bands associated with the 'free' and hydrogen bonded OD groups. The DFT calculations predict relative energies that differ by only 0.6 kJ mol^{-1}.

Vibrational spectra and structural dynamics at elevated temperatures.

The inter-ring hydrogen bonding, which supports the intrinsic *cis* conformation of cellobiose at low temperature in the gas phase, creates an inherently rigid structure. If hydrogen bonding were reduced or more labile at more elevated temperatures, however, this structure might relax into other forms. To explore this possibility, Car-Parinello molecular dynamics simulations were conducted for cellobiose and its singly and doubly (H_2O) hydrated complexes, based in each case, upon the structures determined experimentally at low temperature, T~10K. In cellobiose, the rise in temperature did excite some additional OH (and to a lesser extent CH) motion, which led to brief loss and reconstitution of intramolecular OH-O hydrogen bonds, but nonetheless, the sharp spectral features were retained. Cellobiose, in the gas phase, preserves its rigid *cis* conformational structure at temperatures ≤ 300K; this remained the case even when calculations were run at 600K, although there was some torsional motion of the glycosidic bond. This indicates perhaps, that the *cis* to *trans* transition is governed by the barrier between the minima rather than their energy differences.

The same was broadly true for the monohydrate, but the OH motions, particularly those involving intermolecular interactions with the water molecule, were much more strongly excited at 300K. At 40K little changed over a period ~5 ps. The

water molecule remained in its minimum energy location, forming a stable bridge between OH4' and O6' and, with the exception of OH6' and OH3 (involved in the inter-ring hydrogen-bonding), the other ('spectator') OH groups were also stable. The OH6'→O6 and OH3→O2' hydrogen bonds occasionally cleaved and reformed during the observation period, reflected in the signatures of their associated vibrational modes, σ6' and σ3, which presented a band spectrum characterized by two or more peaks of comparable intensity. At 300K, the sharp 'spectator' bands in the OH spectrum lying above 3600 cm^{-1} showed little change but the bands lying below 3500 cm^{-1}, associated with the hydrogen bonded OH groups, merged into a complex broad feature peaking between 3400 cm^{-1} and 3450 cm^{-1}. The structural changes which these reflect are presented graphically in the series of snapshots taken along the MD trajectories, shown in Figure 4. They include changes in rotamer configuration and the loss/reconstitution of both internal hydrogen-bonds and those involving the water molecule – but throughout these events the global *cis* glycosidic conformation does not change.

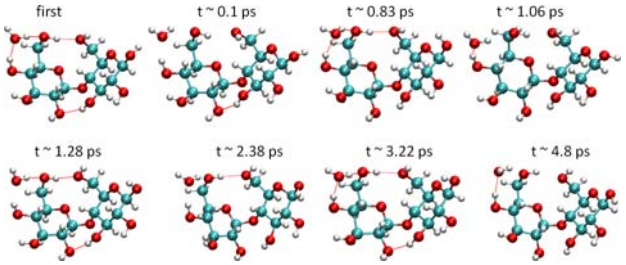

Figure 4. Snapshots of MD trajectories for cellobiose•H_2O, calculated at T ~ 300K. Note the rapid fluctuations in both intermolecular and intramolecular hydrogen bonding.

The Car-Parrinello simulations conducted for cellobiose•$(H_2O)_2$, at T~300K, predicted very similar behavior, see figure 5. The structure remains very rigid at T~40K; at the elevated temperature, despite an increase in the complexity of the OH (and CH) vibrational spectra the structure of the dihydrate was still broadly retained. Various hydrogen bonds can be seen to cleave and reform in the series of snapshots shown in Figure 5, but although the water molecules begin to move and rotate, the $(H_2O)_2$ bridge is maintained throughout the entire trajectory and so too, as before, is the *cis* configuration about the glycosidic linkage.

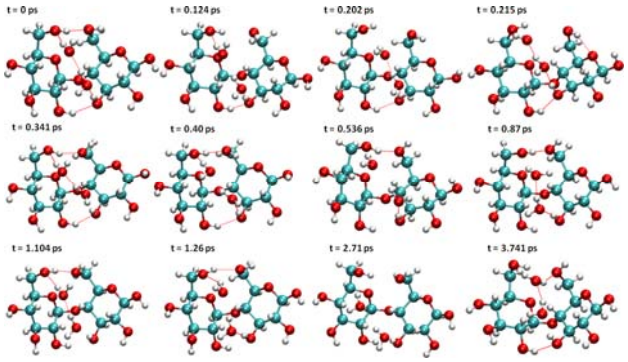

Figure 5. Snapshots of MD trajectories for cellobiose•$(H_2O)_2$, calculated at T~300K.

Conclusions

The isolated and hydrated cellobiose and lactose units both present remarkably rigid structures: their glycosidic linkages adopt a "*cis*" (*anti*-ϕ and *syn*-ψ) conformation bound by inter-ring hydrogen bonds. This conformation is maintained when the temperature is increased to ~300K and it continues to be maintained when the cellobiose (or lactose) unit is hydrated by one or two explicitly bound water molecules. Despite individual fluctuations in the intra- and inter-molecular hydrogen bonding pattern and some local structural motions, the water molecules remain locally bound and the isolated carbohydrates remain trapped within the *"cis"* potential well. The Car-Parrinello dynamical simulations do not suggest any accessible pathway to the *trans* conformations which are formed in aqueous solution and are widespread in nature. Perhaps yet further hydration in the gas phase might move the system beyond the tipping point but for the moment, the issue remains an open one. The retention of the *cis* conformation in the isolated β cellobiose *motif*, even when it binds two water molecules, deepens the mystery of its assuming a *trans* conformation when incorporated as the basic building block in β cellulose, implying a need for the intervention, perhaps, of the biological catalyst promoting cellulose biosynthesis.

Acknowledgements

We appreciate the support provided by the Laser Support Facility of the STFC (JPS), EPSRC for an LSI Platform grant (BGD), the US Department of Energy Office of Science, Grant Number DE-FG02-09ER64762 and the NERSC computational facilities. We also thank the Leverhulme Trust for the award of an Emeritus Fellowship (JPS) and the Royal Society for a Wolfson Research Merit Award (BGD).

References

1. M. Pincu, E. J. Cocinero, N. Mayorkas, B. Brauer, B.G. Davis, R.B. Gerber and J. P. Simons, *J. Phys. Chem. A,* (Pratt Special Issue), 2011, published online, May 13th, 2011.
2. E.C. Cocinero, E.C. Stanca-Kaposta, M. Dethlefsen, B. Liu, D.P. Gamblin, B.G. Davis and J.P. Simons, *Chem. Eur. J.*, 2009, **15**, 13427-13434.
3. E.J. Cocinero, D.P. Gamblin, B.G. Davis and J.P. Simons, *J. Amer. Chem. Soc.*, 2009, **131**, 11117-11123.

Optical trapping of sub-micron liquid aerosol droplets

Andy Ward *andy.ward@stfc.ac.uk*

Andy Ward

Lasers for Science Facility
Research Complex at Harwell, OX11 0FA

Martin King

Department of Geology, Royal Holloway University of London
Egham, Surrey, TW20 0EX

Introduction

Laser tweezers have become increasingly popular[1-3] in the study of atmospheric aerosol science because of the unique way that individual micron-scale aerosol droplets can be trapped and retained for periods of several hours. Recent work has highlighted that there is a correlation between the size of the trapped particle and the laser power required to trap the particle[3]. An important outcome of the study was the observation that conventional single-beam gradient optical trapping becomes unstable when the particle diameter is reduced to below 2 microns. This finding has a significant impact, for aerosol science, as sub-micron aerosol particulates are abundant in the atmosphere. We report our investigations into trapping aerosol droplets in this size range. Sub-micron particles are of interest as they play a key role in the light scattering behaviour of clouds. In addition, when following reaction kinetics on single droplets, there are size-dependent uptake parameters that can reveal whether the reaction occurs inside the droplet or at its surface. Studying a wider range of sizes will assist in the characterization of atmospheric reaction processes.

Experimental

An on-going study in the LSF laboratories has investigated the trapping sub-micron particles using an asymmetric counter-propagating optical trap. The lasers beams are aligned vertically through two objective lenses. A 514.5 nm laser propagates upwards to form a conventional single beam gradient trap using a 63x NA1.2 lens. The lens is also used for imaging and collecting Raman scattered light from the trapped object for acquisition of Raman spectra. A 1064 nm laser is used in the counter-propagating beam (i.e. the downward direction) and is focused using a NA0.45 lens. The numerical aperture is insufficient to form a gradient trap thus the main function of the laser is to supplement the gravitational downward forces by adding a radiation pressure contribution controlled by laser power. The foci of the laser beams are superimposed in the x,y coordinates and separated by 0 to 40 microns in the z-axis using a differential micrometer to control separation.

The aerosol chamber was a custom-made aluminium cell (volume ~8 cm^3), with two borosilicate cover-slips to allow transmission of the counter-propagating beams and illumination light. Attached to this were two aluminium tubes; one for input of the aerosol and gases, and one for exhaust. The input contained a combination of two flows: a constant humidified nitrogen flow, created by bubbling pure nitrogen through water (~1 cm^3 min^{-1}), and a stream of aerosol particles produced using an ultrasonic nebuliser. An aqueous solution of 20 g l^{-1} sodium chloride was nebulised using an ultrasonic nebuliser. The droplet sizes produced were less than 7 micron. Sub-micron droplets were found to be resident in the cell for longer and optical trapping of small droplets occurred 2-5 minutes after the nebulizer was stopped.

Droplets of varying sizes were trapped, as shown in Figure 1, and each was held for at least 20 minutes to allow equilibration with the relative humidity in the chamber. Careful balancing of the opposing laser powers enabled droplets to be captured and focused by slight alteration of the position in the z-axis. For each droplet ratio of laser powers from the upward pointing laser to the downward laser determined. The ratio of trapping beam power to counter-propagating beam power was varied between 0.01 and 2.0.

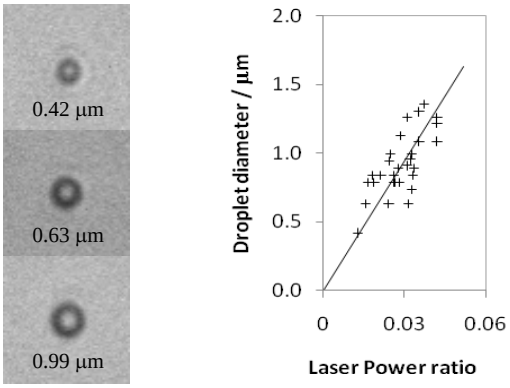

Figure 1. (Left) Examples of droplet images in optical focus when using the counter-propagating laser tweezers system. (Right) Linear dependence of estimated droplet size with the laser power ratio for droplets below 2 microns.

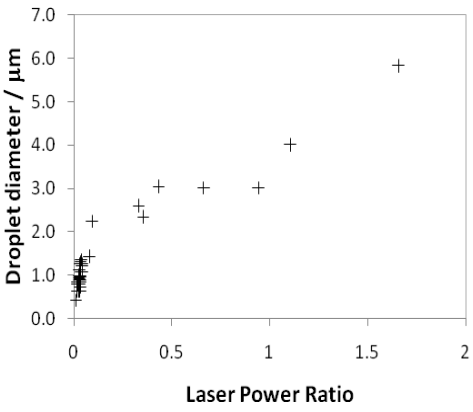

Figure 2. Dependence of estimated droplet size with the laser power ratio for droplets from 0.4 to 6 microns. The plot illustrates the critical point, below the 2 micron region, where significantly greater downward pressure is essential for capturing aerosol droplets.

Sizing of aerosol droplets

There are significant sources of error that arise in determining the droplet size of objects that approach the resolution limit of

the optical microscope. In this study the combined resolution limit of the CCD and microscope is 0.4 µm. Droplets smaller than those shown in Figure 1 are trapped but appear blurred and these are not reported in the sizing data.

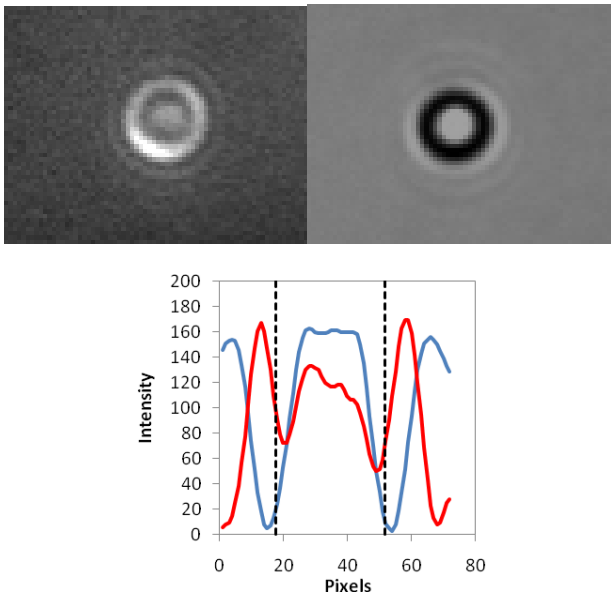

Figure 3. Images of a polystyrene bead under darkfield (top left) and brightfield (top right) illumination. The plot below shows the pixel intensity distribution in relation to the true particle size.

The problem of obtaining accurate sizes from optical images is common and to illustrate the problem images of a 1 µm diameter polystyrene bead are displayed in darkfield and brightfield illumination (Figure 3). A cross-section of the pixel intensity distribution shows the intensity gradients responsible for the visible edges. The actual particle size from the manufacture specification is shown as the dashed line. The darkfield threshold boundary (dark-to-light edge moving outwards from the centre of the particle) overestimates particle diameter by approximately 10 %. The edge of the Airy disc pattern from brightfield imaging overestimates the size by nearly 50%. Polystyrene latex beads from 0.5 to 8.9 µm were characterized in this way and a correction applied to the images of the aerosol droplets. It is appreciated that whilst a linear correction can be determined for polystyrene beads of different sizes the imaging conditions for aerosol droplets is different. Factors such as the refractive index of object, refractive index of the surrounding medium and the exact position of the object in the optical focus are sufficiently different that this correction can, at best, only provide an estimate of droplet size.

Quantitative Raman spectroscopy for size determination

A novel method for the precise measurement of particle diameter (±2 nm) has been developed using cavity resonance behavior inside the droplet[4], however for particles of submicron diameter the signal-to-noise is reduced and the resonances are broad making sizing difficult.

An alternative approach, that is available on the apparatus in the LSF, is to use the Raman spectra acquired from the droplet as a quantitative measurement for determining particle volume. The Raman spectra of the polystyrene beads, used above, were acquired at constant laser power and the intensity of the 1001 rel. cm^{-1} peak was recorded after subtracting background. The dependence of intensity on particle size is shown in Figure 4. A similar dataset was obtained for aerosol salt water droplets using the 3200 rel. cm^{-1} water peak and where particle size was initially estimated from the optical image. The datasets were superimposed by re-scaling the Raman intensities with the aim of demonstrating that similar behavior was occurring in both samples.

The Raman intensity data appears to indicate that for particles t larger than the focal spot size there is a linear dependence between particle diameter and intensity. Thus, it is not the volume of the particle that is important. It is speculated that the focal profile, which is elongated in the vertical plane, is intersecting an approximately cylindrical region of the particles. The dependence of intensity on radius may indicate that increasing particle size increases the length of the cylinder from which Raman scattering originates. At sizes below the focal spot size, there is a relative loss in Raman intensity as a fraction of the laser is no longer incident on the particle. In this region it is likely that there is volume dependence. From this data the focal spot size is 0.9 µm.

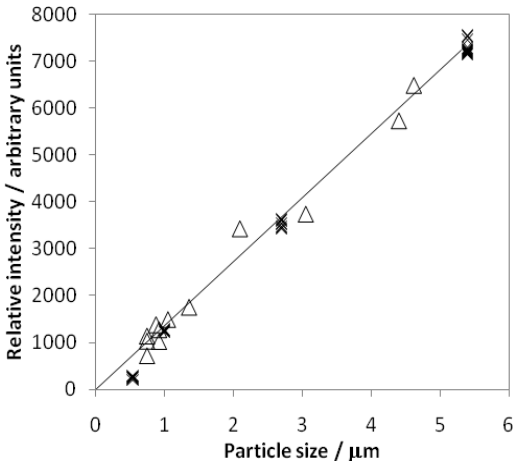

Figure 4. Dependence of the Raman spectral intensity for polystyrene beads (X) and salt water droplets (△) with particle size. The line is a best fit of Raman intensity for sizes above 0.9 microns.

Conclusions

Using the counter-propagating laser trapping configuration, particles can be captured with sizes from about 0.4 µm to more than 6 µm. Further studies are required to refine the quantitative Raman technique, however the initial studies show promise and indicate that sizing of sub-micron aerosol droplets is realistic. The extension in the trapping diameter range for aerosol particles will have application in determining hygroscopicity curves, described by Köhler theory, for proxies of atmospheric aerosol. The laser trapping set-up can be applied for studying cloud droplet diameters of approximately 1 µm.

Acknowledgements

We would like to thank the STFC for providing funding through the Strategic Initiative Program Grant (HS30635)

References

1. M. D King, K.C. Thompson, and A.D. Ward, *J. Am. Chem. Soc.* 126, 51, 16710-6711 (2004)
2. L. Mitchem and J. P. Reid, *Chem. Soc. Rev.* 37, 756-769 (2008).
3. D. McGloin, D. R. Burnham, M. D. Summers, D. Rudd, N. Dewar, and S. Anand, *Faraday Discuss.* 137, 335-350 (2008)
4. A. D. Ward, M. Zhang, and O. Hunt, *Optics Express*, 16, 21, 16392, 2008